Nanoscale Advances

ROYAL SOCIETY OF CHEMISTRY

PAPER

View Article Online
View Journal | View Issue

Cite this: *Nanoscale Adv.*, 2024, **6**, 902

Phase tunable nickel doped Mn_3O_4 nanoparticle synthesis by chemical precipitation: kinetic study on dye degradation

Jasim Uddin,[a] Rahim Abdur,[a] Md. Rifat Hossain,[a] Shahin Aziz,[b] Mohammad Shah Jamal,*[a] Md. Aftab Ali Shaikh*[cd] and Mosharof Hossain *[a]

Nickel (Ni) doped Mn_3O_4 nanoparticles (NPs) were synthesized by a quick and facile chemical precipitation technique to investigate their performance in the degradation of methylene blue (MB) in the absence of light. XRD, FESEM, TEM, AAS, XPS, and FT-IR were used for the investigation of the structural, surface morphological, and elemental composition of Ni doped Mn_3O_4 NPs. XRD confirms the formation of a tetragonal phase structure of pure Mn_3O_4 and 1% and 3% Ni doped Mn_3O_4 NPs. However, mixed phases were found in the case of 5 to 10% Ni doped Mn_3O_4 NPs. Well-defined spherical-shaped morphology was presented through FESEM. Particle sizes decreased linearly (58.50 to 23.68 nm) upon increasing the doping concentration from 0% (pure Mn_3O_4) to 7% respectively, and then increased (48.62 nm) in the case of 10% doping concentration. TEM further confirmed spherical shaped 32 nm nanoparticles for 7% Ni doped Mn_3O_4. The elemental composition and oxidation state of the prepared NPs were confirmed by using XPS spectra. Mixed valence Mn^{2+} and Mn^{4+} states were found in pure Mn_3O_4 and 1% and 3% Ni doped Mn_3O_4 NPs in the ratio of $2MnO–MnO_2$. In addition, three different oxidation states Mn^{2+}, Mn^{3+}, and Mn^{4+} were found in 5 to 10% Ni doped Mn_3O_4 NPs. Moreover, as a dopant Ni exists as Ni^{2+} and Ni^{3+} states in all Ni doped Mn_3O_4 NPs. The synthesized NPs were then applied as potent oxidants for the degradation of MB at pH 3. With the increase of doping concentration to 7%, the degree of degradation was increased to 79% in the first 10 min and finally, it became about 98%. The degradation of MB follows the pseudo-first-order linear kinetics with a degradation rate of 0.0342 min^{-1}.

Received 7th September 2023
Accepted 14th December 2023

DOI: 10.1039/d3na00754e

rsc.li/nanoscale-advances

Introduction

The current intense scientific interest in nanoparticle research is concentrated on metals with remarkable viability to synthesize a broad variety of oxide compounds.[1] Manganese oxides have attracted a lot of interest in recent years due to their physical and chemical characteristics and their prospective uses in solar energy conversion,[2] ion exchange,[3] heterogeneous catalysts,[4] molecular adsorption,[5] electrochemical materials,[6] *etc.* Manganese oxides form several phases like MnO, MnO_2, Mn_2O_3, and Mn_3O_4. Among them, Mn_3O_4 (hausmannite, trimanganese tetraoxide) is one of the most stable mixed oxides at high temperatures and has a spinel structure.[7,8] Due to the presence of various oxidation states of manganese in Mn_3O_4, it can be used as an effective catalyst for the oxidation of methane and carbon monoxide[9] and the selective reduction of nitrobenzene.[10] Additionally, it is a useful compound for reducing nitrogen oxides (NO_x) and volatile organic compound (VOC) emissions from various origins and mitigating air pollution.[11] Because of its various applications, scientists are trying to enhance their activity. Many researchers have already synthesized Mn_3O_4 nanoparticles by using various methods including thermal decomposition,[12] ultrasonic bath,[13] sol–gel,[14] co-precipitation,[15] microwave irradiation,[16] surfactant assisted,[17] oxidation,[18] and physical evaporation.[19] Most of these procedures involve several steps or call for a high vacuum system, a longer reaction time, and oxygen protection.[20] Thus, it is crucial to develop a low-cost, affordable synthetic approach. Chemical precipitation is an easy, inexpensive, and non-toxic approach compared to previously reported methods.[21] Keeping this fact in mind, in this study, Mn_3O_4 and Ni doped Mn_3O_4 nanoparticles with varying doping concentrations were synthesized for the first time using a simple chemical precipitation technique. The fundamental advantage of this technique is that it produces final particles in nanometer dimension with limited size distribution. Nowadays, doping is a promising technique for altering nanomaterials to improve their electrical,

[a]*Institute of Energy Research and Development, Bangladesh Council of Scientific and Industrial Research (BCSIR), Dr Qudrat-i-Khuda Road, Dhanmondi, Dhaka – 1205, Bangladesh. E-mail: msjdubd@gmail.com; mosharof@bcsir.gov.bd*

[b]*BCSIR Laboratories Dhaka, Bangladesh Council of Scientific and Industrial Research (BCSIR), Dr Qudrat-i-Khuda Road, Dhanmondi, Dhaka 1205, Bangladesh*

[c]*Bangladesh Council of Scientific and Industrial Research (BCSIR), Dr Qudrat-i-Khuda Road, Dhanmondi, Dhaka – 1205, Bangladesh. E-mail: aftab74@yahoo.com*

[d]*Department of Chemistry, University of Dhaka, Dhaka – 1000, Bangladesh*

optical, and catalytic properties.[22] Doping of transition metal in Mn-oxide NPs is one of the efficient methods to produce deformed Mn(III) species, which is a crucial structural feature to increase catalytic activity.[23] Since Ni exhibits the highest activity as a dopant of Mn-oxide NPs, in this study Ni doped Mn_3O_4 NPs are synthesized with varying concentrations of dopants.

During the dyeing process, about 15% of the world's total dye production is wasted and discharged in textile effluents.[24] Even at low concentrations, dyes pose a serious threat to aquatic life and human health because they include poisonous and harmful chemical components.[25] Photosynthesis in aquatic plants is impeded by dyes in water, which reduce light transmission. In addition, several of the dyes are said to be very carcinogenic and have poor biodegradability.[26] Methylene blue (MB) is a well-known, highly carcinogenic thiazine pollutant that has been produced and utilized in numerous industries for a variety of reasons. When ingested, it becomes a major risk to human health and has been known to cause damage to the nervous system and eyes.[27] Therefore, researchers are very concerned with finding a quick and efficient way to remove dye and organic contaminants from industrial effluents.[28] Because of their high reduction potential, manganese oxides are powerful oxidants that can easily oxidize a variety of inorganic substances including Cr(III),[29] Sb(III),[30] Co(III),[31] Se(IV),[32] and organic compounds such as catechol, quinines, substituted phenols, aromatic amines, pesticides, and explosives (*e.g.* TNT).[33–38] Many researchers studied the degradation of MB using Mn_3O_4, however the rate of degradation was slow and took a long time.[39,40] In order to overcome these limitations, Ni doped Mn_3O_4 and Mn_3O_4 NPs for MB degradation were prepared. However, various methods such as adsorption,[41] biodegradation,[42] chlorination, and ozonation[43] have been used to remove dyes. In the present study, advanced oxidation technology[44] has been used for comparing the oxidative degradation of MB by newly prepared different concentrations of Ni doped Mn_3O_4 and Mn_3O_4 nanoparticles. The primary aim of this work was to synthesize Ni doped Mn_3O_4 and Mn_3O_4 nanoparticles using a facile chemical precipitation technique for dye (MB) removal from textile effluents. The outcome of this research work will introduce a new dimension in nanoparticle synthesis and find a potential application for the degradation of dyes present in colored aqueous effluents from textile industries.

Experimental

Materials

All chemicals and solvents were purchased and utilized as obtained without further purification. Manganese(II) acetate tetrahydrate (MAct), nickel acetate tetrahydrate (NAct), sodium hydroxide (NaOH), methylene blue, and ethanol were purchased from Sigma-Aldrich Co. Germany.

Preparation of precursor solutions

36.7635 g of MAct salt was dissolved in 500 mL de-ionized (DI) water for the preparation of 300 mM MAct solution. Similarly, 300 mM of NAct solution was prepared by dissolving 7.4652 g NAct salt in 100 mL DI water. Furthermore, a 300 mM NaOH solution was prepared for precipitation by dissolving 12 g pellets in 1000 mL DI water. For better dissolution, all solutions were kept on continuous magnetic stirring at 450 rpm at room temperature.

Synthesis of nanoparticles

The NPs were prepared by a simple inexpensive chemical precipitation technique.[8] For Mn_3O_4 nanoparticle synthesis, 100 mL of freshly prepared MAct solution was taken in a glass beaker. Then NaOH was added at a rate of 6 drops per minute to the precursor solution with continuous magnetic stirring at 450 rpm for allowing precipitation at room temperature. After complete precipitation, the precipitate (ppt) was filtered with Whatman filter paper. The ppt was rinsed with DI water. The rinse was repeated about 5 times to completely remove NaOH. There was no need to put any control over the pH of the solution in this process. Then the ppt was dried in an oven at 90 °C temperature for 24 h. The dried ppt was then weighed and ground into fine powder using a ball miller (Pulverisette 23, FRITSCH, Germany) at 50 Hz for 5 min with 20 balls. Then the powder was taken into quartz crucibles and calcined at 500 °C for 2 h inside a programmable muffle furnace and then slowly cooled down to room temperature. Samples were stored in a vial and kept in a desiccator.

For 1, 3, 5, 7, and 10% Ni doped Mn_3O_4 NP synthesis, 1, 3, 5, 7, and 10 mL NAct solution was taken in a separate glass beaker respectively. Then the volume of each beaker was made to 100 mL by adding the corresponding amount of MAct solution. Other processes were similar to those of Mn_3O_4 NPs. Finally, the NPs were used for different types of characterization.

Characterization

The obtained products were characterized by various characterization techniques. X-ray diffraction (XRD) (EMMA; GBC Scientific Equipment, Australia) patterns were recorded using Cu Kα radiation ($\lambda = 0.15406$ nm) at 35.5 kV and 28 mA, scanning range of 10–70°, at 5° per minute. HighScore software was used to determine the crystallographic data. Surface morphology of the NPs was determined by applying field emission scanning electron microscopy (FESEM); (JSM-7610F, JEOL, Japan) with accelerating voltage: 15 kV, magnification: 1 000 00× and transmission electron microscopy (TEM); (JEM 2100plus, JEOL, Japan). The compositional study of the prepared nanoparticles was carried out by X-ray photoelectron spectroscopy (XPS), (K-alpha, Thermo Fisher Scientific, USA) and atomic absorption spectroscopy (AAS); (AA-7000, Shimadzu, Japan). A study using Fourier transform-infrared spectroscopy (FT-IR) (Frontier, PerkinElmer, UK) was carried out on KBr pellets to characterize distinct surface functionalities in the samples. A UV-vis spectrophotometer (Cintra 2020; GBC Scientific Equipment, Australia) was used to observe the degradation of MB spectroscopically.

Analytical method

First of all, a 500 mL volumetric flask containing 25 mg of MB was filled up to the mark with deionized water (DI) to prepare

a 50 ppm MB solution. A glass beaker was then filled with 100 mL of a produced 50 ppm MB dye solution for the decolorization experiment. The pH of the dye solution was kept at 3. After that, 10 mg of Mn_3O_4 NPs were added to the dye solution with stirring at room temperature in the absence of light. The NPs were left behind as the precipitate after centrifuging 5 mL of the mixed solution for 10 min at the specified time interval. After that, the progress of decolorization was assessed using a UV-vis spectrophotometer. Similarly, MB degradation capacity was measured by using Ni doped Mn_3O_4 nanoparticles keeping the constant amounts of nanoparticles and dye concentration.

Results and discussion

Characterization of Mn_3O_4 and Ni doped Mn_3O_4 nanoparticles

X-ray diffraction (XRD) analysis. The phase and purity of the synthesized Mn_3O_4 and Ni doped Mn_3O_4 nanoparticles were identified by XRD studies. Fig. 1 depicts their obtained diffraction patterns. The diffraction peak positions of Mn_3O_4, 1%, and 3% Ni doped Mn_3O_4 were obtained at 2θ values of 18.1°, 29°, 31.2°, 32.4°, 36.2°, 38.2°, 44.5°, 50.9°, 54°, 56.1°, 58.7°, 60°, and 64.8° corresponding to crystal planes (101), (112), (200), (103), (211), (004), (220), (105), (312), (303), (321), (224) and (400) respectively. All the reflections are perfectly coinciding with the reported tetragonal structure of Mn_3O_4 nanoparticles (JCPDS card no. 024-0734).[8] For 1% and 3% Ni doped Mn_3O_4 nanoparticles, a single phase indicates that Ni is effectively doped into the Mn_3O_4 lattice. However, in the case of 5%, 7%, and 10% Ni doped Mn_3O_4 mixed phases are found. The tetragonal phase structure of Mn_3O_4 (JCPDS card no. 024-0734) and the spinel phase structure of $NiMn_2O_4$ (JCPDS card no. 71-0852) are formed. The diffraction peaks at $2\theta = 30.1°$, 36°, 43°, 57.1°, and 62.8 correspond to the (220), (311), (400), (511), and (440) planes of $NiMn_2O_4$. The above results are in good agreement with the recent study.[23] However, due to the very broad and low intensity of diffraction peaks, the prepared nanoparticle size should be very small.[45] The average crystallite size of prepared Mn_3O_4 and Ni doped Mn_3O_4 NPs was calculated using the Debye–Scherrer equation[46] as follows

$$D = \frac{k\lambda}{\beta \cos \theta}$$

where k is the shape factor (0.94), λ is the X-ray wavelength (1.5418 Å), β is the full width at half maxima (FWHM) of the corresponding diffraction line and θ is the diffraction angle. The average crystallite size, FWHM, peak position, and microstrain calculated for the plane (211) of each sample are shown in Table 1.

It is found that without 1%, the most intense diffraction peak of doped nanoparticles is shifted. As doping concentrations increase from 0% (pure Mn_3O_4) to 7%, the FWHM of the prominent peaks rises respectively, which can be attributed to a reduction in crystallite size. However, in the case of 10% doping concentration, the opposite phenomena are found. Therefore, the broadening and shifting of the diffraction peak with Ni doping strongly suggest that Ni ions have effectively supplanted the Mn ions within the Mn_3O_4 lattice. The reason for the reduced sizes of the Ni doped Mn_3O_4 NPs (from 1 to 7%) is thought to be either oxygen desorption or the fact that Ni, which is injected, settles within the Mn_3O_4 lattice and so forms bonds with the unstable oxygen atoms of Mn_3O_4. This suggests that Ni doping can reduce the nucleation rate of Mn_3O_4 and in turn, can subsequently influence the size of the particles.[47] Microstrain values indicate that with increasing the concentration of dopants, the internal stress is increased. But in the case of 10% doping concentration, the crystallite size suddenly increases which means that it experiences lower internal stress due to the formation of mixed phases.[48,49]

Fourier-transform infrared spectroscopy (FT-IR) analysis. The FT-IR spectra depicted in Fig. 2 supplied crucial characteristic information for the identification of Mn_3O_4 and Ni

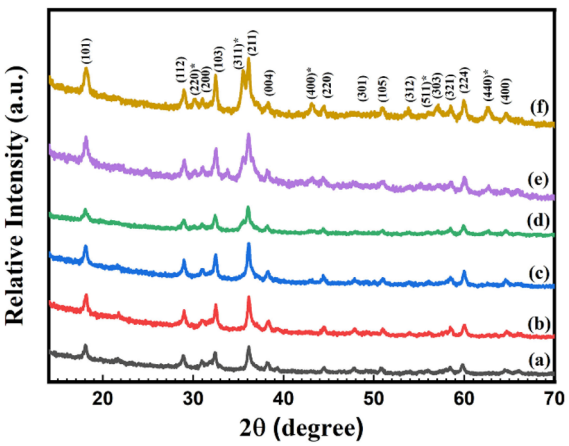

Fig. 1 X-ray diffraction (XRD) patterns of synthesized (a) pure Mn_3O_4, (b) 1% Ni doped Mn_3O_4, (c) 3% Ni doped Mn_3O_4, (d) 5% Ni doped Mn_3O_4, (e) 7% Ni doped Mn_3O_4 and (f) 10% Ni doped Mn_3O_4 NPs.

Table 1 Peak position, FWHM, crystallite sizes, and microstrain of prepared nanoparticles

Nanoparticles	Peak position 2θ (°)	FWHM, β (°)	Crystallite size (nm)	Microstrain (ε) $\times 10^{-3}$
Pure Mn_3O_4	36.16	0.2509	34.81	3.35
1% Ni doped Mn_3O_4	36.16	0.2598	33.62	3.47
3% Ni doped Mn_3O_4	36.12	0.2705	32.29	3.62
5% Ni doped Mn_3O_4	36.06	0.3788	23.05	5.08
7% Ni doped Mn_3O_4	36.12	0.5087	17.17	6.81
10% Ni doped Mn_3O_4	36.14	0.2181	40.05	2.92

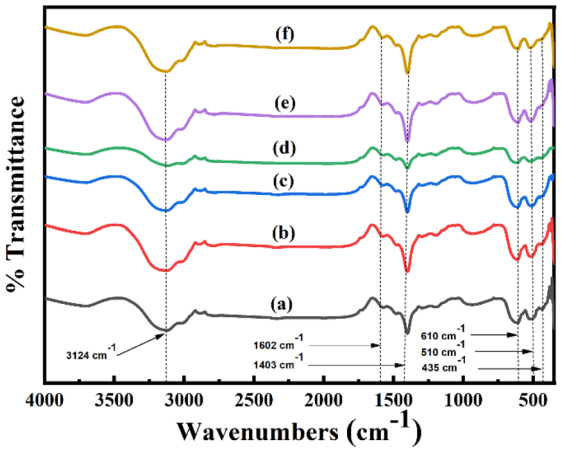

Fig. 2 FT-IR spectra of synthesized (a) pure Mn_3O_4, (b) 1% Ni doped Mn_3O_4, (c) 3% Ni doped Mn_3O_4, (d) 5% Ni doped Mn_3O_4, (e) 7% Ni doped Mn_3O_4 and (f) 10% Ni doped Mn_3O_4 NPs.

doped Mn_3O_4 NPs at various doping levels. The characteristic peaks at 435 cm^{-1}, 510 cm^{-1} and 610 cm^{-1} could be linked with the stretching vibrations of Mn–O and Ni–O bonds. Moreover, the broad band near 3124 cm^{-1} shows O–H stretching and the low intense band located at 1602 cm^{-1} shows the bending vibration of O–H groups in the adsorbed water molecules. Additionally, the band located at 1403 cm^{-1} matches the coordination bond of Mn by O–H. However, the FT-IR spectra of the prepared NPs show a notable resemblance with the previous results.[8,22]

X-ray photoelectron spectroscopy (XPS) analysis. XPS spectra as shown in Fig. 3 were used to further evaluate the elemental composition and oxidation state of the prepared nanoparticles. The XPS of Mn 2p of Mn_3O_4 and 7% Ni doped Mn_3O_4 NPs are shown in Fig. 3a and b respectively. In addition, binding energies of Ni 2p of 7% Ni doped Mn_3O_4 are shown in Fig. 3c. Due to spin–orbit splitting Mn, the 2p peak generates two possible states as $2p_{3/2}$ and $2p_{1/2}$. The deconvoluted spectrum of Mn 2p (Fig. 3a) resulted in four peaks. Among these, two peaks at 640.5 eV (Mn $2p_{3/2}$) and 652.1 eV (Mn $2p_{1/2}$) correspond to the Mn^{2+} state, while the other two peaks at 642.5 eV (Mn $2p_{3/2}$) and 654.1 eV (Mn $2p_{1/2}$) are attributed to the Mn^{4+} state. As the peak ratio of Mn^{2+} is almost two times greater than that of Mn^{4+}, the composition of the oxide would be $2MnO–MnO_2$. These results agree well with the values reported in the literature.[50] The above results are similar for 1% and 3% Ni doped Mn_3O_4 also. However, in the case of 5 to 10% Ni doped Mn_3O_4 NPs, three types of oxidation states are found due to the change of phase. The deconvoluted spectrum (Fig. 3b) of Mn 2p of 7% Ni doped Mn_3O_4 shows six peaks. Among these, two peaks at 640.8 and 652.4 eV are associated with the Mn^{2+} state, while the other two peaks at 644.4 and 654.6 eV are associated with the Mn^{3+} state. Again, the Mn^{4+} state is responsible for two broad peaks at 642.1 and 653.6 eV. There are four peaks visible in the Ni 2p spectrum (Fig. 3c) of 7% Ni doped Mn_3O_4 NPs after deconvolution. Two peaks at 854.2 and 872 eV correspond to the Ni^{2+} state while the other two peaks at 859.9 and 878.3 eV are attributed to the Ni^{3+} state.[51]

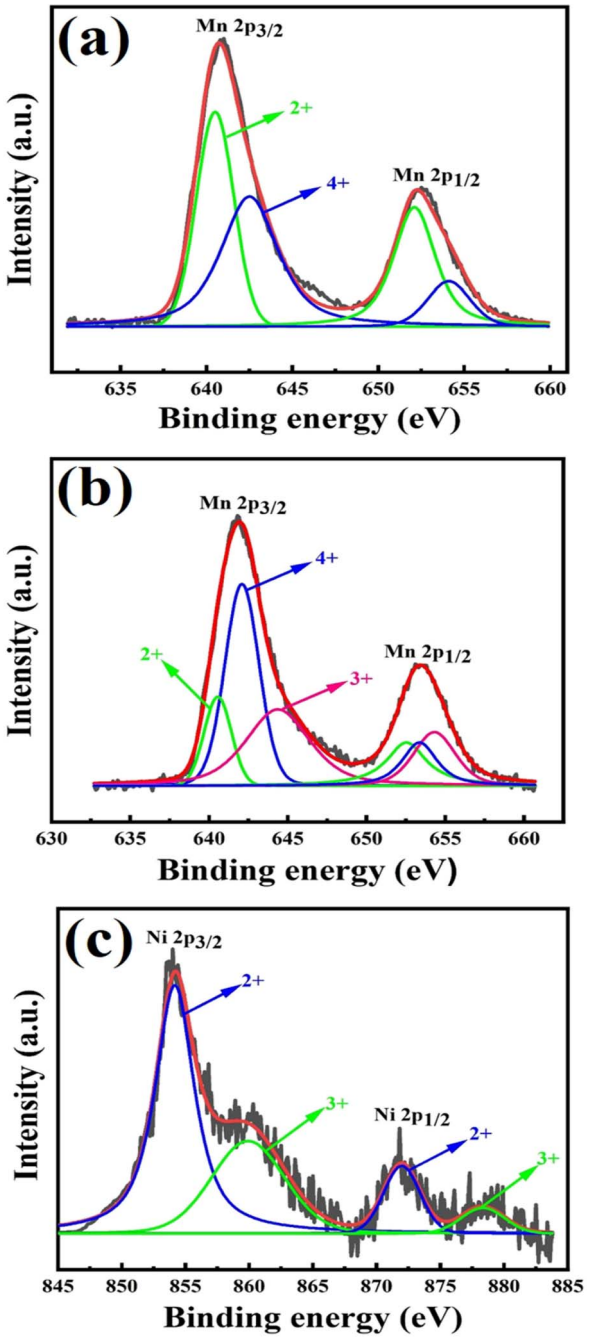

Fig. 3 XPS spectra of (a) Mn 2p of pure Mn_3O_4, (b) Mn 2p of 7% Ni doped Mn_3O_4 and (c) Ni 2p of 7% Ni doped Mn_3O_4 NPs.

Field emission scanning electron microscopy (FESEM) analysis. The surface morphology and particle size of the synthesized nanoparticles were investigated based on FESEM images shown in Fig. 4a–f. Grains with smaller sizes are distributed randomly for all cases. It can also be seen that NPs are well defined as spherical-shaped particles with the size decreasing from 58.5 nm to 23.68 nm with increasing doping concentration up to 7% and then increasing to 48.62 nm in the case of 10% doping concentration. The estimated values from the XRD pattern and these measurements are in good agreement.

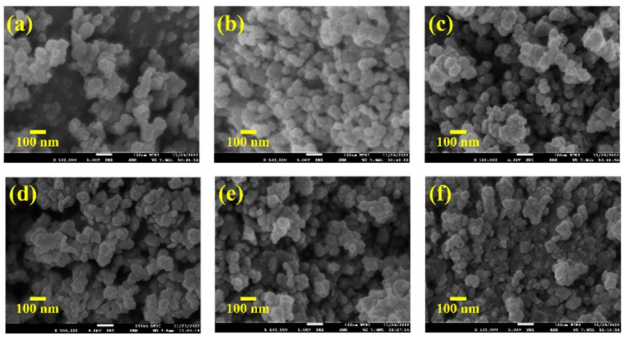

Fig. 4 FESEM images of (a) pure Mn_3O_4, (b) 1% Ni doped Mn_3O_4, (c) 3% Ni doped Mn_3O_4, (d) 5% Ni doped Mn_3O_4, (e) 7% Ni doped Mn_3O_4 and (f) 10% Ni doped Mn_3O_4 NPs.

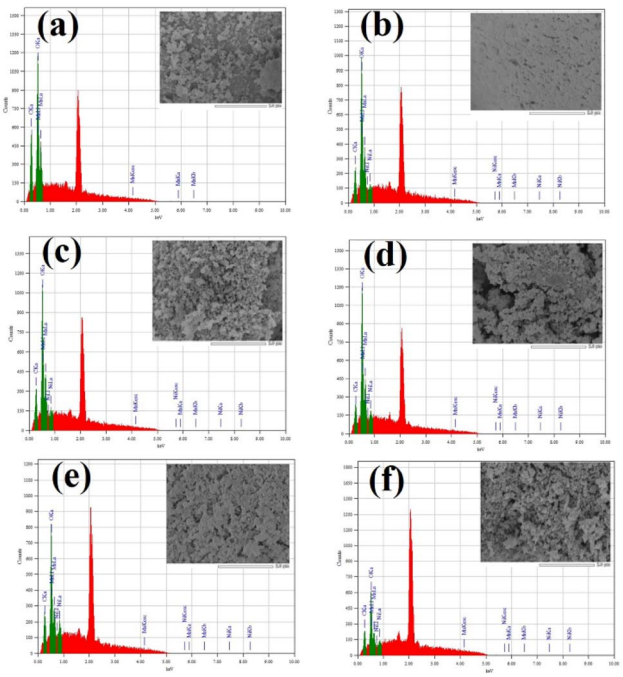

Fig. 5 EDS mapping of synthesized (a) pure Mn_3O_4, (b) 1% Ni doped Mn_3O_4, (c) 3% Ni doped Mn_3O_4, (d) 5% Ni doped Mn_3O_4, (e) 7% Ni doped Mn_3O_4 and (f) 10% Ni doped Mn_3O_4 NPs.

The EDS analysis was also carried out for the elemental composition of the prepared NPs which is shown in Fig. 5a–f. In the case of pure Mn_3O_4 NPs, only Mn and O atomic percent values were found (Fig. 5a). On the other hand, Ni doped Mn_3O_4 NPs showed elemental peaks of Mn, Ni and O (Fig. 5b–f). The average values of atomic percent of constituent atoms with standard deviation are presented in Table 2. The Ni atomic percent increased with increasing Ni doping percent, though the atomic percent of Ni does not directly delineate the original doping percent, but rather illustrates the increasing trend.

The elemental peak of carbon was found in each EDS spectrum because carbon tape was used for attaching the sample during FESEM and EDS analysis.

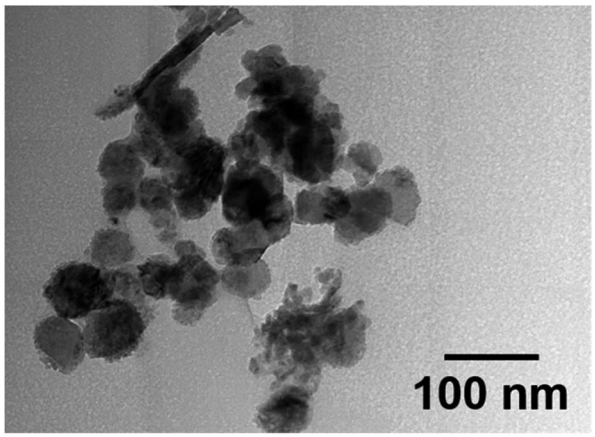

Fig. 6 TEM image of 7% Ni doped Mn_3O_4 NPs.

Transmission electron microscopy (TEM) analysis. The 7% Ni doped Mn_3O_4 NPs were analysed using TEM to visualize the actual particle size and shape (Fig. 6). The result showed spherical shaped particles with size distribution. The average particle size was determined to be approximately 32 nm.

Atomic absorption spectroscopy (AAS) analysis. All the samples were further analysed using AAS to confirm the weight percent of Mn and Ni present in the samples. 0.03 g of each sample was dissolved in concentrated HNO_3 acid by heating at 200 °C for 2 h and then stock solution and 100 and 1000 times dilution solutions were prepared using DI water. Finally the dilution solutions were characterized using AAS for Mn and Ni elements, each sample at least three times. The results are tabulated in Table 3.

Effect of particle size of pure Mn_3O_4 and Ni doped Mn_3O_4 NPs on MB degradation. Effect of particle size of pure Mn_3O_4 and Ni doped Mn_3O_4 NPs on MB degradation was also examined. The following equation[44] was employed to determine the rate of MB degradation at various reaction times:

Table 2 Elemental composition of prepared NPs obtained by EDS analysis

	Atomic percent (%)			
Nanoparticles	Mn	Ni	O	C
Pure Mn_3O_4	37.31 ± 0.79	Not detected	39.40 ± 2.22	23.29 ± 2.54
1% Ni doped Mn_3O_4	41.06 ± 0.58	0.88 ± 0.04	44.12 ± 0.57	13.94 ± 0.04
3% Ni doped Mn_3O_4	40.79 ± 0.26	2.41 ± 0.38	42.91 ± 0.19	13.89 ± 0.60
5% Ni doped Mn_3O_4	40.78 ± 0.10	4.43 ± 0.28	44.42 ± 0.07	10.37 ± 0.25
7% Ni doped Mn_3O_4	37.65 ± 1.05	6.63 ± 0.11	40.55 ± 0.35	15.17 ± 0.63
10% Ni doped Mn_3O_4	35.86 ± 1.16	8.97 ± 0.45	41.53 ± 0.18	13.63 ± 1.44

Table 3 Elemental composition of prepared NPs obtained by AAS analysis

	Atomic percent (%)	
Nanoparticles	Mn	Ni
Pure Mn_3O_4	28.492 ± 0.008	Not detected
1% Ni doped Mn_3O_4	28.575 ± 0.033	0.600 ± 0.002
3% Ni doped Mn_3O_4	28.658 ± 0.017	1.879 ± 0.003
5% Ni doped Mn_3O_4	27.450 ± 0.050	3.758 ± 0.003
7% Ni doped Mn_3O_4	25.925 ± 0.008	4.626 ± 0.007
10% Ni doped Mn_3O_4	26.017 ± 0.050	5.232 ± 0.012

$$\text{Degree of degradation } (\%) = \frac{A_0 - A}{A_0} \times 100$$

where A_0 is the initial absorbance and A is the absorbance at time t of MB. Fig. 7 displays the degradation of 50 ppm MB solution using pure Mn_3O_4 and Ni doped Mn_3O_4 NPs at pH 3. It is noted that pure Mn_3O_4, 1, 3, 5, 7, and 10% Ni doped Mn_3O_4 removed 59, 61, 68, 69, 79, and 69% of MB after the first 10 min respectively. Hence, it is clear that the MB degradation efficiency increases with doping concentration up to 7% due to the decreasing of particle sizes. Additionally, when the particle size decreased, both the total number of active sites on the surface and the particular surface area of the NPs rose, which might significantly boost the efficiency of MB decolorization.[38] But in the case of 10% doping concentration, MB degradation percentage decreased because of increasing particle size. Finally, for pure Mn_3O_4 NPs, about 95% and for Ni doped Mn_3O_4 NPs about 98% of MB were degraded. When compared to the scientific literature, these outcomes are comparatively superior to those of zinc oxide (60%), nano cadmium sulfide (29%), zinc sulfide (27%), Mn_3O_4/Fe_2O_3 (85%), Mn_3O_4/Fe_3O_4 nanocomposites (93%), zinc sulfide/cadmium sulfide composites (85%), hollow cadmium sulfide nanospheres (87%), commercial anatase (73%), cadmium sulfide −6, 8, 18 (96%) and photolysis only (21%); and lower than that of graphene–zinc oxide (100%).[39,40,44,52–55] Theoretically, at pH < 4.5, protonation causes the surface of Mn_3O_4 to become positively charged. As pH decreases, the positive charge of Mn_3O_4 increases, which inhibits the adsorption of the cationic dye MB and the creation of the surface precursor due to electrostatic repulsion. As a result, MB was decolorized by Mn_3O_4 following a surface mechanism, *i.e.*, the interaction of MB with surface-bound Mn(II, III) to produce a surface precursor complex, where electron transport takes place.[38,44]

Kinetic study. Kinetic data could be used to determine the oxidative breakdown of MB. The degradation process of MB followed the pseudo-first-order linear kinetics and the findings are presented in Fig. 8. By drawing a graph between the variables $\ln(C_0/C)$ and time (t) of the following equation,[44] the findings of a kinetic analysis of all prepared samples were determined.

$$\ln\left(\frac{C_0}{C}\right) = kt$$

where C_0 is the initial concentration at $t = 0$ and C shows the concentration at time t, whereas the slope of the graph shows the rate constant (k). The linear kinetics were evidently being followed by all samples, and 7% Ni doped Mn_3O_4 NPs exhibited the best performance.

These results showed the higher values of rate constants in comparison to recent studies.[38,44,52,56] Furthermore, the larger value of k indicates that the NPs are more appropriate for the decolorization of MB. Rate constants, r^2 values, and degree of degradation (%) of all NPs are given in Table 4.

MB degradation percentage is compared with previously reported values using similar types of doped metal oxide NPs, and the results are tabulated in Table 5.

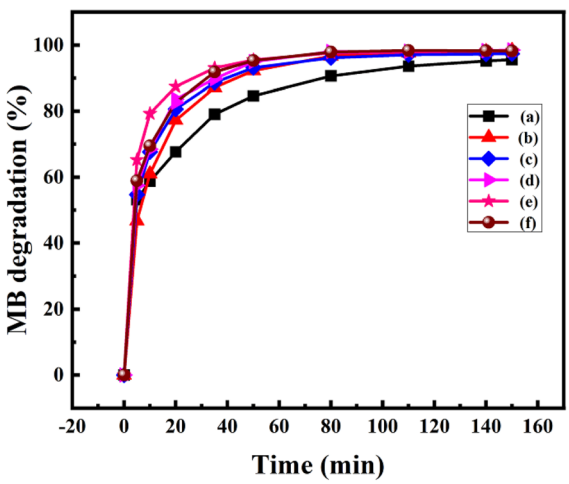

Fig. 7 Effect of particle sizes of (a) pure Mn_3O_4, (b) 1% Ni doped Mn_3O_4, (c) 3% Ni doped Mn_3O_4, (d) 5% Ni doped Mn_3O_4, (e) 7% Ni doped Mn_3O_4 and (f) 10% Ni doped Mn_3O_4 NPs on MB degradation at pH 3.0.

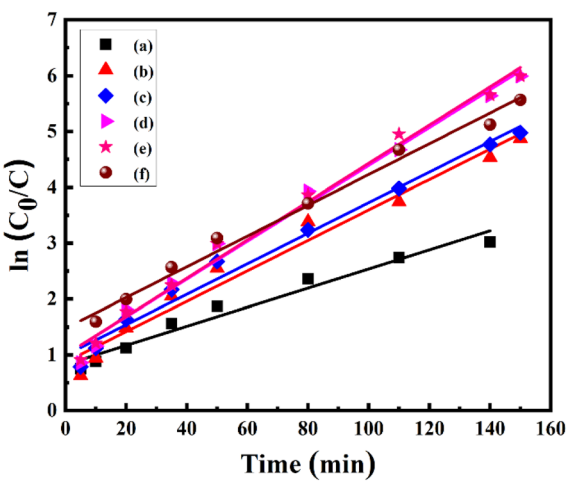

Fig. 8 Pseudo-first-order kinetic model for the degradation of MB using 50 ppm of each (a) pure Mn_3O_4, (b) 1% Ni doped Mn_3O_4, (c) 3% Ni doped Mn_3O_4, (d) 5% Ni doped Mn_3O_4, (e) 7% Ni doped Mn_3O_4 and (f) 10% Ni doped Mn_3O_4 NPs at pH 3.0.

Table 4 Rate constants and degree of degradation of prepared nanoparticles

Nanoparticles	MB concentration (ppm)	Degree of degradation (%)	r^2	Rate constants (min^{-1})
Pure Mn_3O_4	50	95	0.968	0.0171
1% Ni doped Mn_3O_4		98	0.973	0.0272
3% Ni doped Mn_3O_4		98	0.983	0.0273
5% Ni doped Mn_3O_4		98	0.989	0.0339
7% Ni doped Mn_3O_4		**98**	**0.990**	**0.0342**
10% Ni doped Mn_3O_4		98	0.989	0.0275

Table 5 Comparison of MB degradation performance

Materials	MB degradation percentage	References
Pure Mn_3O_4	80%	44
Te-doped Mn_3O_4	82%	57
Peroxymonosulfate/Mn_3O_4	86.71%	28
Mn_3O_4/Fe_3O_4 nanocomposites	93%	52
Mn_3O_4/ZnO	94.59%	58
Samarium-doped Mn_3O_4	95.4%	59
Ni doped Mn_3O_4 NPs	**98%**	**This work**

Conclusions

Ni doped Mn_3O_4 NPs with different Ni percentages were successfully synthesized through a simple chemical precipitation technique. The particle size observed using FESEM was reduced from 58.50 to 23.68 nm when dopants were incorporated into the Mn_3O_4 matrix from 0% to 7% respectively. However, in the case of 10% doping concentration, the particle size was increased to 48.62 nm. Further TEM analysis confirmed spherical shaped NPs with an average size of 32 nm for 7% Ni doped Mn_3O_4. The composition of the elements in the prepared NPs was confirmed by the XPS data. Pure Mn_3O_4, 1% and 3% Ni doped Mn_3O_4 NPs were shown to have Mn^{2+} and Mn^{4+} states and 5 to 10% of Ni doped Mn_3O_4 NPs contained three different oxidation states, including Mn^{2+}, Mn^{3+}, and Mn^{4+}. Furthermore, all doping NPs contain nickel as a dopant in the Ni^{2+} and Ni^{3+} states. By changing the percentage of dopants, the phase of the prepared NPs can be easily tuned. The Ni-doping process leads to the change of phases of NPs which increased the decolorization rate. But the excess incorporation of dopants (10%) increased the crystallite size and decreased the degradation rate of MB. The kinetic study confirmed that all synthesized products followed the pseudo-first-order linear kinetics, and 7% Ni doped Mn_3O_4 showed a higher degradation rate of 0.0342 min^{-1} among all samples. It showed an excellent degradation rate because of the lower size and higher surface area of particles. A major advantage of the Ni doped Mn_3O_4 NPs was found to be the rapid degradation of dye compared to Mn_3O_4. Due to the high degradation rate, Ni doped Mn_3O_4 NPs will create a new dimension for the purification of dye polluted wastewater in the world.

Author contributions

Conceptualization: MH; methodology: JU, MH; experimental: JU, RA; data curation: JU, RA; formal analysis: MRH, RA, JU; writing the main manuscript: JU, MH; reviewing the manuscript: SA, AAS, MSJ; all authors have read and agreed to the published version of the manuscript.

Conflicts of interest

The authors declare that they have no conflict of interest.

Acknowledgements

The authors are grateful for the assistance of Riyadh Hossen Bhuiyan, Scientific Officer, BCSIR Laboratories, Dhaka, and Md. Saiful Quddus, senior Scientific Officer, Institute of Glass & Ceramic Research and Testing (IGCRT), BCSIR, Dhaka-1205, Bangladesh. The authors declare that this manuscript was prepared under the R&D project of "Incorporation of inorganic hole-transporting materials (HTL) for efficient and stable perovskite solar cells".

References

1 Y. Wang, C. Hou, X. Lin, H. Jiang, C. Zhang and G. Liu, *Appl. Phys. A: Mater. Sci. Process.*, 2021, **127**, 1–7.
2 Y. Yamashita, K. Mukai, J. Yoshinobu, M. Lippmaa, T. Kinoshita and M. Kawasaki, *Surf. Sci.*, 2002, **514**, 54–59.
3 Q. Feng, H. Kanoh and K. Ooi, *J. Mater. Chem.*, 1999, **9**, 319–333.
4 T. Rhadfi, J. Y. Piquemal, L. Sicard, F. Herbst, E. Briot, M. Benedetti and A. Atlamsani, *Appl. Catal., A*, 2010, **386**, 132–139.
5 Y. F. Shen, R. P. Zerger, R. N. DeGuzman, S. L. Suib, L. McCurdy, D. I. Potter and C. L. O'Young, *Science*, 1993, **260**, 511–515.
6 A. R. Armstrong and P. G. Bruce, *Nature*, 1996, **381**, 499–500.
7 M. Mansournia, F. Azizi and N. Rakhshan, *J. Phys. Chem. Solids*, 2015, **80**, 91–97.
8 B. Gnana Sundara Raj, A. M. Asiri, J. J. Wu and S. Anandan, *J. Alloys Compd.*, 2015, **636**, 234–240.
9 E. R. Stobbe, B. A. De Boer and J. W. Geus, *Catal. Today*, 1999, **47**, 161–167.
10 E. J. Grootendorst, Y. Verbeek and V. Ponec, *J. Catal.*, 1995, **157**, 706–712.
11 M. F. M. Zwinkels, S. G. JÄRÅS, P. G. Menon and T. A. Griffin, *Catal. Rev.*, 1993, **35**, 319–358.
12 O. Jankovský, D. Sedmidubský, P. Šimek, Z. Sofer, P. Ulbrich and V. Bartuněk, *Ceram. Int.*, 2015, **41**, 595–601.

13 T. Rohani Bastami and M. H. Entezari, *Ultrason. Sonochem.*, 2012, **19**, 560–569.
14 M. Mohamed Ismail, S. Hemaanandhan, D. Mani, M. Arivanandhan, G. Anbalagan and R. Jayavel, *J. Sol-Gel Sci. Technol.*, 2020, **93**, 703–713.
15 A. K. Singh, T. K. Dhiman, G. B. V. S. Lakshmi, R. Raj, S. K. Jha and P. R. Solanki, *Nanotechnology*, 2022, **33**, 285501.
16 T. V. M. Sreekanth, Y. Kisoo and J. Kim, *Int. J. Energy Res.*, 2022, **46**, 1683–1692.
17 L. Laffont and P. Gibot, *Mater. Charact.*, 2010, **61**, 1268–1273.
18 K. A. M. Ahmed, Q. Zeng, K. Wu and K. Huang, *J. Solid State Chem.*, 2010, **183**, 744–751.
19 Y. Q. Chang, X. Y. Xu, X. H. Luo, C. P. Chen and D. P. Yu, *J. Cryst. Growth*, 2004, **264**, 232–236.
20 Z. Durmus, H. Kavas, A. Baykal and M. S. Toprak, *Cent. Eur. J. Chem.*, 2009, **7**, 555–559.
21 A. Ramadoss, K. Krishnamoorthy and S. J. Kim, *Mater. Res. Bull.*, 2012, **47**, 2680–2684.
22 A. K. Worku, D. W. Ayele and N. G. Habtu, *SN Appl. Sci.*, 2021, **3**, 1–16.
23 J. S. Hong, H. Seo, Y. H. Lee, K. H. Cho, C. Ko, S. Park and K. T. Nam, *Small Methods*, 2020, **4**, 1–7.
24 A. Houas, H. Lachheb, M. Ksibi, E. Elaloui, C. Guillard and J. M. Herrmann, *Appl. Catal., B*, 2001, **31**, 145–157.
25 L. Hu, G. Deng, W. Lu, Y. Lu and Y. Zhang, *Cuihua Xuebao*, 2017, **38**, 1360–1372.
26 S. C. DeVito, *Crit. Rev. Environ. Sci. Technol.*, 1993, **23**, 249–324.
27 M. I. Din, R. Khalid, J. Najeeb and Z. Hussain, *J. Cleaner Prod.*, 2021, **298**, 126567.
28 R. Shokoohi, M. Khazaei, K. Godini, G. Azarian, Z. Latifi, L. Javadimanesh and H. Zolghadr Nasab, *Inorg. Chem. Commun.*, 2021, **127**, 108501.
29 J. G. Kim, J. B. Dixon, C. C. Chusuei and Y. Deng, *Soil Sci. Soc. Am. J.*, 2002, **66**, 306–315.
30 N. Belzile, Y. W. Chen and Z. Wang, *Chem. Geol.*, 2001, **174**, 379–387.
31 A. Manceau, V. A. Drits, E. Silvester, C. Bartoli and B. Lanson, *Am. Mineral.*, 1997, **82**, 1150–1175.
32 M. J. Scott and J. J. Morgan, *Environ. Sci. Technol.*, 1996, **30**, 1990–1996.
33 C. J. Matocha, D. L. Sparks, J. E. Amonette and R. K. Kukkadapu, *Soil Sci. Soc. Am. J.*, 2001, **65**, 58–66.
34 R. A. Petrie, P. R. Grossl and R. C. Sims, *Environ. Sci. Technol.*, 2002, **36**, 3744–3748.
35 H. Li, L. S. Lee, D. G. Schulze and C. A. Guest, *Environ. Sci. Technol.*, 2003, **37**, 2686–2693.
36 H. Zhang and C. H. Huang, *Environ. Sci. Technol.*, 2005, **39**, 4474–4483.
37 K. H. Kang, D. M. Lim and H. Shin, *Water Res.*, 2006, **40**, 903–910.
38 M. X. Zhu, Z. Wang and L. Y. Zhou, *J. Hazard. Mater.*, 2008, **150**, 37–45.
39 X. Li, Y. Gao, L. Yu and L. Zheng, *J. Solid State Chem.*, 2010, **183**, 1423–1432.
40 A. Wei, L. Xiong, L. Sun, Y. Liu, W. Li, W. Lai, X. Liu, L. Wang, W. Huang and X. Dong, *Mater. Res. Bull.*, 2013, **48**, 2855–2860.
41 M. Arshadi, M. Mehravar, M. J. Amiri and A. R. Faraji, *J. Colloid Interface Sci.*, 2015, **440**, 189–197.
42 A. T. Moore, A. Vira and S. Fogel, *Environ. Sci. Technol.*, 1989, **23**, 403–406.
43 Y. M. Slokar and A. Majcen Le Marechal, *Dyes Pigm.*, 1998, **37**, 335–356.
44 A. K. M. Atique Ullah, A. K. M. Fazle Kibria, M. Akter, M. N. I. Khan, A. R. M. Tareq and S. H. Firoz, *Water Conserv. Sci. Eng.*, 2017, **1**, 249–256.
45 Y. Li, H. Tan, X. Y. Yang, B. Goris, J. Verbeeck, S. Bals, P. Colson, R. Cloots, G. Van Tendeloo and B. L. Su, *Small*, 2011, **7**, 475–483.
46 V. Maruthapandian, T. Pandiarajan, V. Saraswathy and S. Muralidharan, *RSC Adv.*, 2016, **6**, 48995–49002.
47 G. Raja, A. Nallathambi, A. Prakasam, S. Gopinath, C. Ragupathi, S. Narayanan, P. Tamizhdurai, R. Kumaran, N. S. Alsaiari, K. M. Abualnaja and M. Ouladsmane, *J. Saudi Chem. Soc.*, 2022, **26**, 101440.
48 S. Karpagavalli, S. J. Kennady Vethanathan and S. Perumal, *Int. J. Nanopart.*, 2019, **11**, 305–321.
49 W. Qin, T. Nagase, Y. Umakoshi and J. A. Szpunar, *Philos. Mag. Lett.*, 2008, **88**, 169–179.
50 G. An, P. Yu, M. Xiao, Z. Liu, Z. Miao, K. Ding and L. Mao, *Nanotechnology*, 2008, **19**(27), 275709.
51 S. Saha, A. Roy, A. Ray, T. Das, M. Nandi, B. Ghosh and S. Das, *Electrochim. Acta*, 2020, **353**, 136515.
52 G. C. Silva, V. S. T. Ciminelli, A. M. Ferreira, N. C. Pissolati, P. R. P. Paiva and J. L. López, *Mater. Res. Bull.*, 2014, **49**, 544–551.
53 S. Liu, H. Li and L. Yan, *Mater. Res. Bull.*, 2013, **48**, 3328–3334.
54 W. M. Zhang, Y. Q. Jiang, X. Y. Cao, M. Chen, D. L. Ge and Z. X. Sun, *Mater. Res. Bull.*, 2013, **48**, 4379–4384.
55 G. Lin, J. Zheng and R. Xu, *J. Phys. Chem. C*, 2008, **112**, 7363–7370.
56 X. Wang, L. Mei, X. Xing, L. Liao, G. Lv, Z. Li and L. Wu, *Appl. Catal., B*, 2014, **160–161**, 211–216.
57 M. Umar, H. Ajaz, M. Javed, S. Iqbal, M. Shuaib Khan, A. Alhujaily, N. S. Awwad and H. A. Ibrahium, *Inorg. Chem. Commun.*, 2023, **157**, 111353.
58 B. Shaikh, M. A. Bhatti, A. A. Shah, A. Tahira, A. K. Shah, A. Usto, U. Aftab, S. I. Bukhari, S. Alshehri, S. N. U. Shah Bukhari, M. Tonezzer, B. Vigolo and Z. H. Ibhupoto, *Nanomaterials*, 2022, **12**, 3754.
59 M. S. Osgouei, N. Kamrani, S. Fazli-Shokouhi and M. Khatamian, *J. Alloys Compd.*, 2022, **902**, 163729.